Chemical
Science

ROYAL SOCIETY
OF CHEMISTRY

EDGE ARTICLE

View Article Online
View Journal | View Issue

Check for updates

Cite this: *Chem. Sci.*, 2021, **12**, 453

All publication charges for this article have been paid for by the Royal Society of Chemistry

Bridging photochemistry and photomechanics with NMR crystallography: the molecular basis for the macroscopic expansion of an anthracene ester nanorod†

Kevin R. Chalek,[a] Xinning Dong,[a] Fei Tong,[a] Ryan A. Kudla,[a] Lingyan Zhu,[a] Adam D. Gill,[b] Wenwen Xu,[e] Chen Yang,[a] Joshua D. Hartman, [a] Alviclér Magalhães, [c] Rabih O. Al-Kaysi, [d] Ryan C. Hayward, [e] Richard J. Hooley, [a] Gregory J. O. Beran, [a] Christopher J. Bardeen *[a] and Leonard J. Mueller *[a]

Received 15th September 2020
Accepted 29th October 2020

DOI: 10.1039/d0sc05118g

rsc.li/chemical-science

Crystals composed of photoreactive molecules represent a new class of photomechanical materials with the potential to generate large forces on fast timescales. An example is the photodimerization of 9-*tert*-butyl-anthracene ester (**9TBAE**) in molecular crystal nanorods that leads to an average elongation of 8%. Previous work showed that this expansion results from the formation of a metastable crystalline product. In this article, it is shown how a novel combination of ensemble oriented-crystal solid-state NMR, X-ray diffraction, and first principles computational modeling can be used to establish the absolute unit cell orientations relative to the shape change, revealing the atomic-resolution mechanism for the photomechanical response and enabling the construction of a model that predicts an elongation of 7.4%, in good agreement with the experimental value. According to this model, the nanorod expansion does not result from an overall change in the volume of the unit cell, but rather from an anisotropic rearrangement of the molecular contents. The ability to understand quantitatively how molecular-level photochemistry generates mechanical displacements allows us to predict that the expansion could be tuned from +9% to −9.5% by controlling the initial orientation of the unit cell with respect to the nanorod axis. This application of NMR-assisted crystallography provides a new tool capable of tying the atomic-level structural rearrangement of the reacting molecular species to the mechanical response of a nanostructured sample.

1. Introduction

The creation of new stimuli-responsive materials is a central goal in chemistry. Although many such materials are based on polymers, over the last decade molecular crystals have become recognized as dynamic, mechanically responsive structures.[2] Dramatic examples of this dynamic nature involve photomechanical effects, where crystals composed of photochemically reactive molecules undergo a variety of mechanical deformations when exposed to light, including bending,[3–15] twisting,[16–18] peeling,[19,20] and rotational/translational motion.[21–24] In most cases, the photomechanical effect can be understood as resulting from the formation of a bimorph structure within the crystal: spatially distinct regions of incommensurate reactant and product phases lead to interfacial strain that drives the shape change. If the crystal is transformed from 100% reactant to 100% product, there is no interfacial strain and thus no bending.[25,26]

Reactant-product interfacial stress is not the only way to obtain photomechanical motion: a complete single-crystal-to-single-crystal transformation can generate even greater amounts of work *via* expansion. There are many examples of single crystal polymorphic phase transformations that lead to shape changes and mechanical motion.[27–30] These mechanically active crystal transitions usually rely on heat or mechanical stimuli to drive the change in crystal packing arrangements – no

---

[a] *Department of Chemistry, University of California-Riverside, Riverside, CA 92521, USA. E-mail: leonard.mueller@ucr.edu; christopher.bardeen@ucr.edu*

[b] *Department of Biochemistry, University of California-Riverside, Riverside, CA 92521, USA*

[c] *Department of Organic Chemistry, Institute of Chemistry, Federal University of Rio de Janeiro, Rio de Janeiro, RJ, 21941-909, Brazil*

[d] *College of Science and Health Professions-3124, King Saud Bin Abdulaziz University for Health Sciences, King Abdullah International Medical Research Center, Ministry of National Guard Health Affairs, Riyadh 11426, Kingdom of Saudi Arabia*

[e] *Department of Chemical and Biological Engineering, University of Colorado Boulder, 3415 Colorado Ave., Boulder, CO 80303, USA*

† Electronic supplementary information (ESI) available. See DOI: 10.1039/d0sc05118g

actual chemical change takes place, just a shifting of the molecules within the crystal lattice. An analogous phase change can be achieved in a molecular crystal during a photochemical reaction. In this case, molecular photoisomerization changes the local crystal packing, which in turn drives large-scale changes in crystal shape. From a practical standpoint, a negative photochromic system is required in order to achieve full reaction so that the photoproduct does not absorb the incoming light.[31–33] Furthermore, crystal fracture and disintegration are common in macroscopic photoreactive crystals, necessitating the use of micro- or nanoscale crystals in order to limit internal strain build-up.[34–37]

We have developed a family of 9-anthracene esters that undergo a [4 + 4] photodimerization reaction in crystal form,[38] for which 9-*tert*-butyl-anthracene ester (**9TBAE**) is the most studied example. When grown as single-crystal nanorods, the **9TBAE** crystal-to-crystal photodimerization reaction (Fig. 1a) leads to a unique crystal phase – the solid-state reacted dimer (SSRD) – and large expansion along the rod axis with a slight contraction across its diameter. The large directional expansion has the potential to perform linear actuation, similar to the anisotropic expansion of piezoelectric crystals that allows them to function as mechanical actuators. The photoinduced expansion of **9TBAE** nanorods was first observed in 2006,[39] but exactly how the molecular-level geometry changes yield the observed expansion has remained a mystery. In many photomechanical systems, a unit cell expansion/contraction is invoked to qualitatively describe bending phenomena derived from reactant/produce interfacial strain. However, the **9TBAE** system provides a unique case of 100% conversion, so in principle knowledge of the reactant and product crystal structures should allow us to quantitatively predict the expansion. But previous attempts to rationalize the observed photochemical transformation in **9TBAE** nanorods based on changes in the unit cell volume incorrectly predicted that nanorods should shrink by 1.2%, rather than expand by 8%.[40] Clearly, knowledge of the reactant and product crystal structures is not sufficient to predict the photomechanical response of the material.

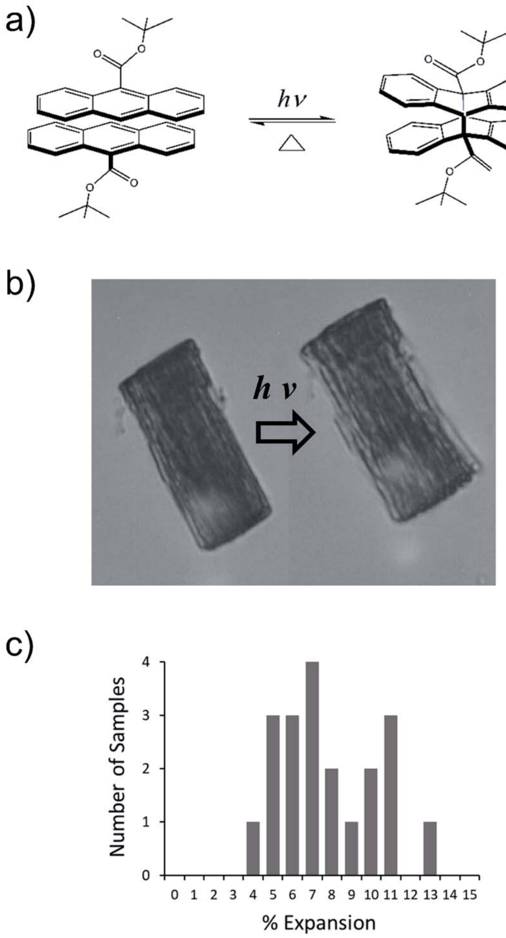

Fig. 1 (a) Photodimerization reaction of 9TBAE. (b) A bundle of 9TBAE nanorods undergoes a photoinduced expansion of 6.9%. (c) Histogram of nanorod bundle expansions measured by optical microscopy before and after 2 minutes of exposure to 365 nm (intensity = 20 mW cm^{-2}).

In favorable cases, traditional single-crystal X-ray diffraction methods can be used to determine the structural rearrangements induced by photodimerization. But the useful photomechanical response only occurs in **9TBAE** nanorods. Larger crystals fragment and disintegrate due to the buildup of internal strain, so a structural characterization method that can be adapted to the nanorod sample is necessary. Furthermore, it is vital to be able to connect crystal structure changes with the photochemical reaction progress. NMR is often used to monitor chemical changes, and although ^{13}C-labeling is usually required to increase sensitivity, it can also be used to assess crystal packing and orientation. In this article, we describe a new approach that combines ensemble oriented-crystal NMR spectroscopy and first-principles computational chemistry to determine the absolute unit cell orientations relative to the shape change in a photoreactive, molecular crystal, **9TBAE** nanorod. Solid-state NMR (SSNMR) has been used to study a number of solid-state photochemical transformations,[25,38,40–52] and foundational work by Nieuwendaal, Hayes and coworkers[53] demonstrated how single-crystal NMR could be used to determine the relative orientation of the reactant and product in the single-crystal to single-crystal topochemical photoreaction of *trans*-cinnamic acid. Our work builds on this approach and for the first time uses SSNMR to tie the atomic-level structural rearrangement of the reacting molecular species to the mechanical response of a nanostructured sample. We deduce the absolute monomer and dimer crystal orientations within the **9TBAE** nanorods and develop a quantitative molecular-level model of the photochemical reaction that predicts a macroscopic elongation of 7.4%, in good agreement with the experimental value. Our analysis demonstrates that both the molecular shape change of the reacting unit and the molecular reorientation relative to the nanoscale crystal must be considered.[54] Based on these observations, we predict that tailoring the alignment of the **9TBAE** monomer crystal unit cell with respect to the nanorod axis can tune the mechanical response from a 9% expansion to a 9.5% contraction. The results demonstrate how the synergistic combination of SSNMR spectroscopy, X-ray diffraction, and first-principles computational chemistry – an integrated approach often referred to as NMR-assisted crystallography[55–69] – can provide crucial insights for engineering new crystal-based responsive materials.

2. Results and discussion

2.1. Nanorod expansion

The expansion of **9TBAE** nanorods grown in an AAO template is a general phenomenon, but there is some variability in the magnitude of the effect, even within a single sample. The photodimerization reaction is illustrated in Fig. 1a. Optical microscopy images of a bundle of rods before and after 365 nm irradiation are shown in Fig. 1b, and a histogram of the expansion for individual nanorods is shown in Fig. 1c. The average expansion is 8 ± 2%, with some expanding as much as 13% and others as little as 5%. Both PXRD and SSNMR measurements have confirmed that the solid-state photodimerization occurs in the AAO growth templates as well, and previous SEM images showed that the nanorods expand vertically even when confined in the template.[39] Therefore, we assume that any insights gained from studies on **9TBAE** nanorods aligned in the AAO template are relevant to the dynamics occurring in individual nanorods as well.

2.2. Unit cell orientations from NMR crystallography

Given that the nanorods expand, the next task is to establish the orientation of the **9TBAE** unit cells with respect to the shape change. SSNMR provides one approach for determining absolute crystal orientation based on the inherent spatial anisotropy of the interactions.[1,70,71] NMR observables such as chemical shift and dipolar coupling depend not only on the local molecular and electronic structure, but also on molecular orientation with respect to the laboratory-frame magnetic field. Measuring chemical shifts as a function of crystal orientation is a classic way to obtain molecular chemical shift tensors and orient them with respect to the crystal and molecular frames.[72] Conversely, if the magnitude and positioning of the relevant tensors within the molecular frame are known, then single-crystal NMR spectra can be used to align the unit cell relative to the magnetic field.[53]

Our previous determination of the monomer and SSRD crystal structures[40] allows the required dipolar and chemical shift tensors to be obtained. Dipolar tensors can be placed directly on the molecular frame based on the molecular coordinates,[1] while chemical shift tensors can be predicted very accurately from the three-dimensional geometry using first-principles computational methods.[73] We recently reported first-principles chemical shifts for the **9TBAE** monomer and SSRD species in the solid state, calculated using DFT.[40,73] These computationally predicted shifts showed good agreement with the experimentally measured isotropic chemical shifts (monomer and SSRD) and chemical shift tensors (SSRD). The tensor components for monomeric **9TBAE** were not part of the previous study, so select tensors were measured and are compared to the first-principles values in the ESI.† The dipolar and shift tensor values are summarized in the ESI† for each of the asymmetric units in the monomer and SSRD unit cells.

In order to establish the dynamic molecular features necessary to model the NMR spectrum, we first investigated a large single crystal of **9TBAE** prepared ^{13}C labeled on the ester moiety *t*-butyl group ($^{13}C_4$-*t*-Bu-**9TBAE**). The ^{13}C solid-state NMR spectrum of this bulk single crystal in Fig. 2 shows two magnetically inequivalent *t*-butyl groups, corresponding to two distinct arrangements of the asymmetric unit relative to the magnetic field. Note that the sample yields a well-resolved spectrum without the customary magic angle spinning because it is a single crystal as opposed to a randomly oriented powder. The spectrum is consistent with fast rotation of the *t*-butyl group about the O–C ester bond, leading to three dynamically-equivalent methyl carbons (centered at 30 ppm) and a simplified multiplet pattern for the two magnetically inequivalent quaternary carbons (centered at 70 and 100 ppm, respectively) that each show an average dipolar coupling to their respective three methyl carbons with a roughly 1 : 3 : 3 : 1 intensity pattern. The methyl resonances in these spectra are more complicated because they are modulated not only by the dipolar coupling back to the quaternary carbon, but also by the ^{13}C dipolar couplings between the three methyl groups; unlike *J*-couplings between magnetically-equivalent sites, these methyl group dipolar couplings do alter the spectrum. Full numerical density matrix simulations of this four-spin system (*vide infra*) support these interpretations.

Knowledge of the chemical shift and dipolar tensors for **9TBAE** allows this spectrum to be used to uniquely align the

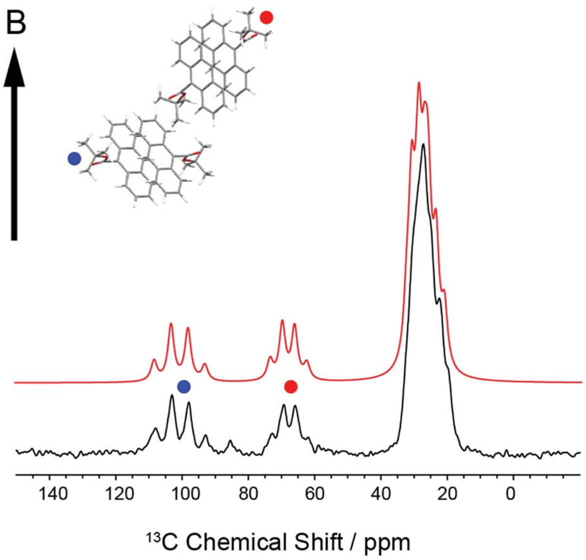

Fig. 2 Experimental ^{13}C solid-state NMR spectrum of a bulk single crystal of $^{13}C_4$-*t*-Bu-**9TBAE** (black) and the best fit spectrum (red) to the alignment of the unit cell relative to the laboratory magnetic field. The two orientations of the asymmetric unit relative to the magnetic field (marked with red and blue dots) give rise to two distinct resonances for the quaternary carbons. This spectrum is consistent with rapid rotation of the *t*-butyl groups about the ester O–C bond, giving three magnetically equivalent methyl groups. The best fit spectrum was generated *via* numerical simulation of the spin dynamics, taking as input the first-principles chemical shift and dipolar tensors.

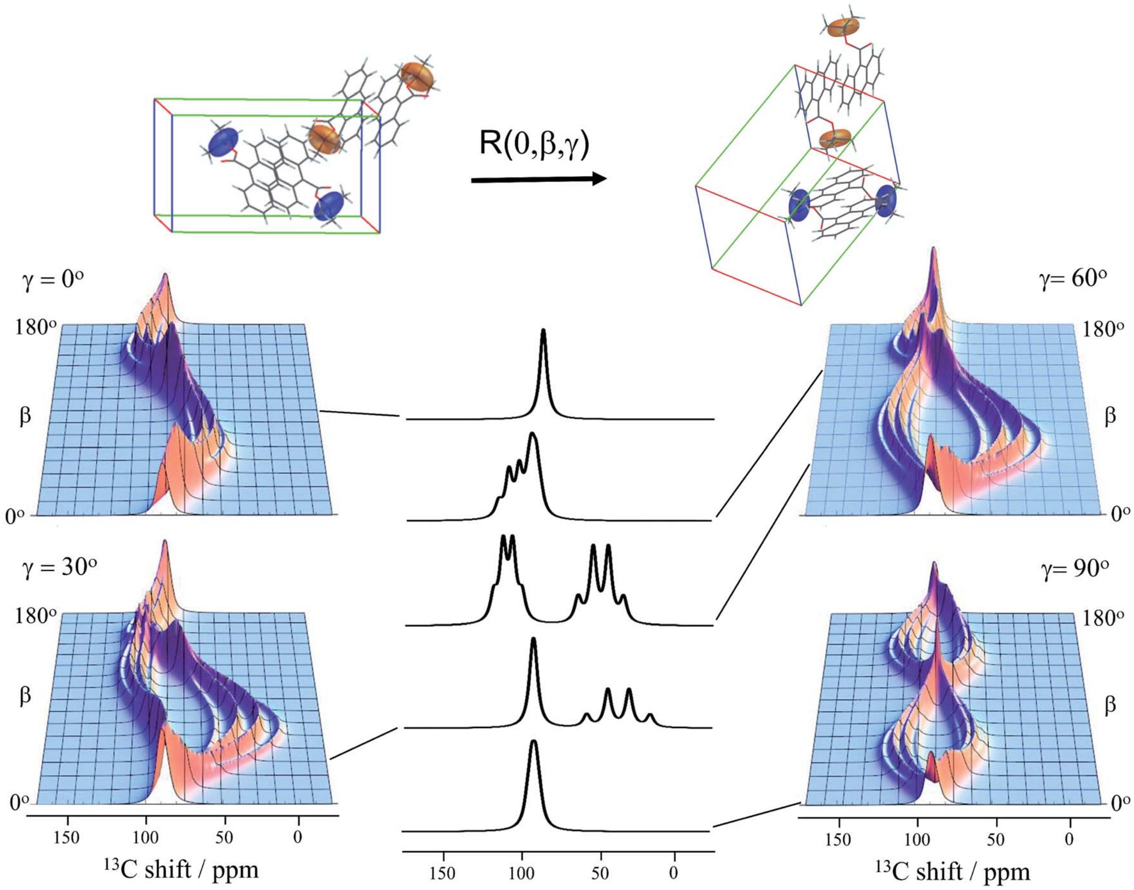

Fig. 3 The predicted $^{13}C_4$-*t*-Bu-**9TBAE** single crystal ^{13}C solid-state NMR spectrum as a function of unit cell orientation relative to laboratory frame magnetic field. In these simulations, only the quaternary carbon resonances are shown and strong coupling effects are neglected. The dipolar and chemical shielding tensors used to generate these simulations were determined *via* first-principle calculations as described in the text and are fixed relative to the unit cell. As the unit cell rotates, the resulting spectral parameters are modulated, giving rise to orientation-dependent spectra. The magnetically equivalent chemical shift tensors for asymmetric units related by inversion symmetry are shown in the same color, while the magnetically inequivalent tensors are colored independently. Molecules and tensors are rendered in TensorView1.4.[1]

crystal relative to the laboratory frame magnetic field. Fig. 3 shows the predicted quaternary carbon NMR spectrum as a function of the unit cell orientation in the laboratory frame, defined by Euler angles β and γ using an active rotation convention.[71] The methyl carbons are omitted for clarity. By scanning these angles to find the best match with experiment, the orientation of the single crystal in the magnetic field can be determined; in this case the crystal frame is rotated from initial alignment with the laboratory frame by Euler angles $\beta = 19.2°$ and $\gamma = 73.8°$ to give its final orientation in the magnetic field. The full dynamically-averaged CSA and dipolar tensors were considered in the four-spin numerical density matrix simulations used to predict the best-fit spectrum shown in Fig. 2.

The data in Fig. 3 show how it is possible to use SSNMR spectra to obtain the absolute orientation of a **9TBAE** crystal with respect to the magnetic field. However, the **9TBAE** nanorods are too small to be studied individually with single-crystal NMR. Rather, a bulk ensemble of uniformly oriented single-crystal nanorods was left within the AAO growth template and placed into a flat coil NMR probe with their rod axes aligned parallel to the static magnetic field. As the nanorods grow normal to the disk-shaped template surface,[39] this uniform alignment was accomplished by positioning the disk perpendicular to the field (Fig. S2†). Fig. 4a shows the resulting ^{13}C solid-state NMR spectrum of the $^{13}C_4$-*t*-Bu-**9TBAE** monomeric nanorods. Although each crystalline nanorod within the template can potentially have a distinct azimuthal displacement, the observed NMR spectrum is insensitive to this angle when the rod axis is aligned along the magnetic field, giving spectra with reasonably good resolution. That a single axis of alignment allows for high resolution NMR studies is well-known in other contexts, such as oriented bilayer systems.[74]

There are several qualitative differences between the single crystal and nanorod spectra. First, the NMR resonances of the nanorod sample are broadened compared to those of the bulk single crystal. This broadening cannot be ascribed to (orientation-dependent) intermolecular dipole–dipole couplings between the ^{13}C-labeled moieties in this static solid as the single crystal spectrum in Fig. 2 was acquired with the same labeling density and shows no such broadening; additional experiments performed on nanorods prepared using 10% labeled monomer confirm this and show this same broad set of

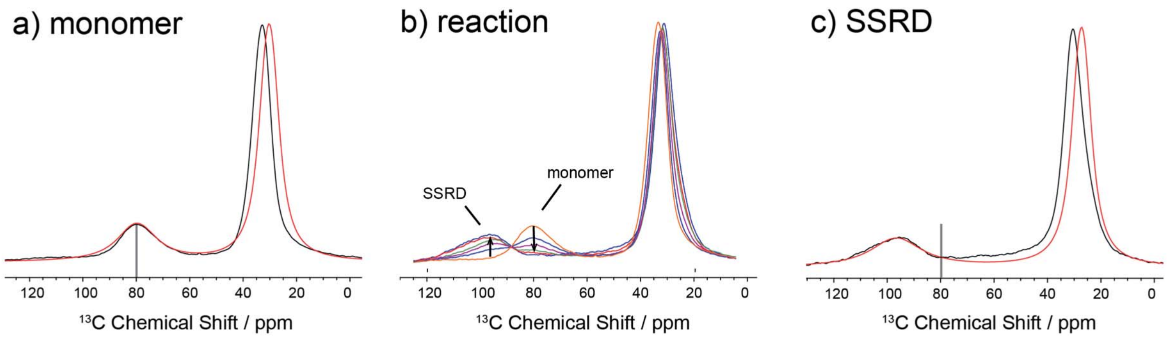

Fig. 4 ^{13}C solid-state NMR spectra of ensemble-oriented $^{13}C_4$-*t*-Bu-**9TBAE** nanorods within an AAO template with the long rod axes parallel to the magnetic field direction. (a) The experimental spectrum of monomeric **9TBAE** (black) and the spectrum for the best fit orientation of its unit cell relative to the magnetic field/rod axis (red). (b) The spectrum of **9TBAE** during progressive periods of UV irradiation shows the transition from the monomer to the solid-state reacted dimer species; spectra correspond to progressive 5 minute periods of irradiation. (c) The experimental spectrum of the SSRD (black) and the spectrum for the best fit orientation of its unit cell relative to the magnetic field/rod axis (red).

resonances (Fig. S10†). Rather, these line widths can be reproduced by assuming a Gaussian distribution of alignment angles with a standard deviation of ±3.6° as detailed in the ESI.† Second, only a single resonance is observed for the quaternary carbons. This places restrictions on the alignment of the monomer unit cells, which must have the previously distinct quaternary carbons in magnetically equivalent orientations. This is confirmed when the unit cells are rigorously oriented with respect to the magnetic field by once more tracking the agreement between the experimental and predicted quaternary carbon spectral frequencies. The error surface (residuals squared) for this analysis is shown in Fig. S7 (ESI†), and the best-fit spectrum in Fig. 4a (red trace) corresponds to an 84.4° rotation of the unit cell along the crystallographic *b* axis with Euler angles $\beta = 84.4°$ and $\gamma = 180°$. For reference, the closest Miller plane perpendicular to the rod axis is (13,0,−1), which is tilted 4° from the (1,0,0) Miller plane and has a normal 5.6° off the real space [1,0,0] axis.

Fig. 4b shows the evolution of the SSNMR spectrum during the photodimerization reaction. After each irradiation period, the sample is removed from the light and placed in the NMR spectrometer to obtain a ^{13}C spectrum. There is a clear transition from the monomer to the SSRD, with the quaternary carbon shifting downfield and broadening slightly, and an isosbestic point is observed, consistent with a two-state single-crystal-to-single-crystal reaction model. While acquisition of these spectra is time-consuming (9 h. each), the integrated NMR signals are proportional to the chemical concentrations (within certain limits under cross-polarization[75,76]) at the end of the irradiation periods, which allows us to quantitatively follow the course of the dimerization reaction. Fig. 4c shows the spectrum of the fully converted SSRD nanorods. As with the monomer, only a single quaternary resonance is observed, signaling that the sites remain magnetically equivalent. Again, the orientation-dependent spectra can be predicted and scanned to determine the alignment of the dimer unit cell in the magnetic field and therefore relative to the rod axis. The error surface for this scan is given in Fig. S8 (ESI†) and the best-fit agreement (red trace, Fig. 4c) corresponds to a 144.5° rotation of the unit cell along the crystallographic *a* axis (Euler angles $\beta = 144.5°$ and $\gamma = 90.0°$). For reference, the nearest low index Miller plane is (0,1,−2), which is tilted 2.3° off of this plane, while the [0,1,−1] real space axis is 2° off of the plane normal.

To confirm the crystal orientations deduced from the SSNMR experiments, GIWAXS measurements were also undertaken on the oriented AAO templates. The GIWAXS experiment acquires diffraction information across a range of angles, so it is sensitive to crystal planes with different orientations with respect to the surface plane. The GIWAXS results show a good match with SSNMR, with absolute alignments differing by only 5.6° for the monomer and 2° for the dimer. The full details of the GIWAXS experiments and their analysis are given in the ESI.†

2.3. Connecting photochemical structural rearrangement to photochemical crystal expansion

Given the absolute crystal orientations before and after the photochemical reaction, the molecular-level basis for the macroscopic response of the **9TBAE** nanorods can be delineated. Our starting point is atomic, focusing on the how photodimerization alters the bonding and structural arrangements. Fig. 5a shows the overlay of the molecular contents in the oriented monomer and SSRD unit cells. While the overall molecular positions overlap almost perfectly, the solid-state [4 + 4] photocycloaddition reaction generates several key atomic displacements that drive the photomechanical response. Note that initially the monomer anthracene rings are packed slightly offset. As the photoreaction occurs, the newly formed carbon–carbon bonds pull the rings into registry, while at the same time the planes bend out to accommodate the new sp^3 hybridization at the central carbons. This "butterfly" motion opens up space above and below the dimers that allows adjacent pairs to stack more efficiently along the direction of the anthracene rings. During this reconfiguration, the *t*-butyl ester groups remain essentially fixed with respect to the anthracene core; this is in contrast to their 180° outward rotation for the polymorph crystallized out of solution.[38] Overall, this minimum displacement reaction pathway is consistent with the *topochemical principle* – the solid-state monomers dimerize with minimal

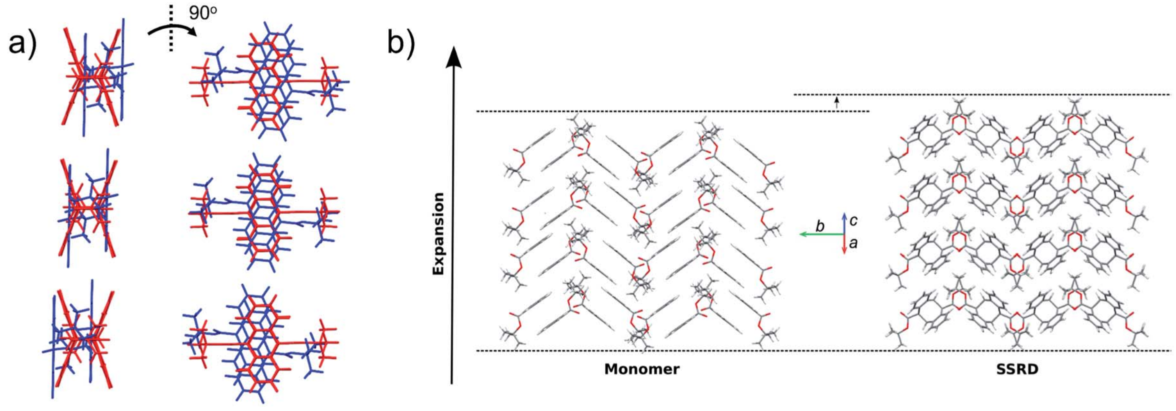

Fig. 5 Molecular geometry and packing changes in crystalline **9TBAE** due to photodimerization. (a) The molecular-level view shows that the anthracene rings of adjacent monomers (blue) are initially offset; after photodimerization, the rings are pulled into registry and the planes bend out to accommodate the new sp^3 hybridization (butterfly distortion). There is also a rectification of the stacking along the direction of the anthracene ring planes. (b) The effect of the molecular geometry changes on the crystal packing at the level of the herringbone pairs shows how the formation of the sp^3 carbons causes the anthracene rings to pucker and push the herringbone layers apart. The net expansion axis is along the diagonal of the monomer unit cell *ac* crystal plane.

disruption to the crystal packing/ester side chain conformations.[77–79] Moving one level out, the effect of these molecular geometry changes on the crystal packing can be seen most clearly by looking at a single layer of herringbone pairs. Fig. 5b shows how the atomic-level reconfiguration translates into a net expansion as the now protruding phenyl groups push the herringbone pairs apart.

The nanorods are three-dimensional macroscopic objects, and the final step is to understand how the herringbone pair expansion projects into this space. Fig. 6 shows the absolute molecular orientations of the monomer and SSRD relative to the nanorod axis, which are key to understanding the photomechanical response. The molecular expansion identified in Fig. 5b lies along the diagonal of the monomer unit cell *ac* plane, but as seen in Fig. 6a only a component of this expansion falls along the nanorod axis. The elongation of the nanorod is aided, however, by a slight tilt of the dimer unit cell as each successive layer of dimers adjusts its position to partially compensate for the expansion of the neighboring herringbone pair. This layer shift also leads to a significant contraction perpendicular to the

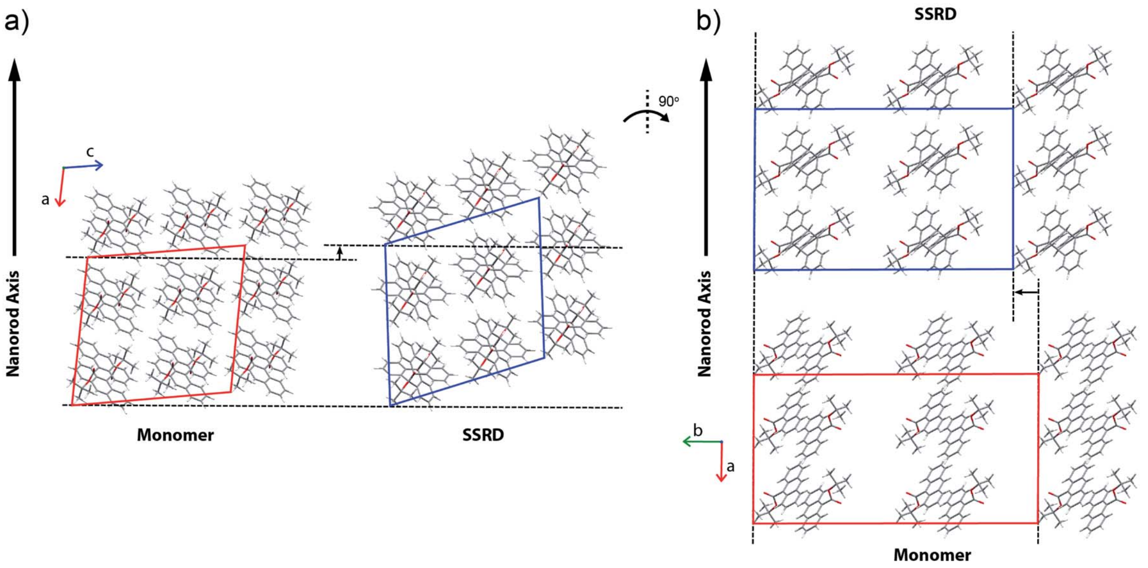

Fig. 6 The orientations of the monomer and SSRD unit cells relative to the nanorod axis. The formation of the dimer pairs manifests as (a) a net expansion along the nanorod axis and (b) a contraction perpendicular. The monomer unit cell is shown in red, while the one-to-one atom mapping of this unit cell onto the SSRD is shown as the *transformed* dimer unit cell in blue. The expansion along the rod axis can be measured as the change in the *z*-projection of a point initially on the nanorod (*z*) axis; this gives a predicted expansion of 7.4%, in good agreement with the experimentally measured distribution. Concomitant with the expansion along the nanorod axis, is a predicted 9.5% contraction along the unit cell *b* axis.

rod axis (Fig. 6b). We had previously observed this contraction but could not absolutely quantify it due to the small feature size (it is harder to resolve a 9% change in 200 nm than an 8% change over 60 μm). According to this analysis, molecular shape change and spatial/unit cell rotation are both operative in the **9TBAE** photomechanical response.

The qualitative observations above on crystal packing changes and mechanical displacements can be quantified in a unit cell based model of the photomechanical single-crystal to single-crystal transformation. During the crystal reconfiguration, the monomer unit cell axes ($\mathbf{a}_\mathrm{m}$, $\mathbf{b}_\mathrm{m}$, and $\mathbf{c}_\mathrm{m}$) morph into the *transformed* dimer unit cell axes ($\mathbf{a}_\mathrm{d}'$, $\mathbf{b}_\mathrm{d}'$, and $\mathbf{c}_\mathrm{d}'$). For a general photoreaction, the transformed axes do not necessarily correspond to the minimum unit cell obtained from a standard XRD analysis, which due to unique symmetries could be drawn quite differently for two species. Rather, the transformed unit cell is chosen to provide a 1-to-1 atom mapping of the monomer to dimer transformation, which facilitates comparisons between the crystal forms; these are the axes shown in Fig. 6. Using this approach, the displacement upon photoreaction of any point in the monomer crystal can be determined by first representing it in fractional coordinates of the monomer unit cell

$$\boldsymbol{r} = u\mathbf{a}_\mathrm{m} + v\mathbf{b}_\mathrm{m} + w\mathbf{c}_\mathrm{m} \tag{1}$$

and then reconstituting it on the transformed dimer axes with the same fractional coordinates

$$\boldsymbol{r}' = u\mathbf{a}_\mathrm{d}' + v\mathbf{b}_\mathrm{d}' + w\mathbf{c}_\mathrm{d}'. \tag{2}$$

here, both the monomer and transformed dimer lattice vectors are written in the nanorod frame, with the absolute orientations determined above. To measure the expansion of the nanorod, we track the *z*-displacement of a point initially on the nanorod *z*-axis. Using this quantitative model, an elongation of 7.4% is predicted as the **9TBAE** monomer converts to the SSRD, in excellent agreement with the experimentally observed value of 8%. At the same time, a contraction of 9.5% is predicted along the diameter of the rod.

As noted above, the broadened NMR resonances for the monomer nanorods can be fit to a Gaussian distribution of alignment angles with a standard deviation of 3.6° for the unit cell relative to the nanorod axis (Fig. S11, ESI†). Based on the assumptions that the relative orientation of the monomer and SSRD unit cells is fixed during the photochemical reaction, this same distribution in the initial orientation of the monomer unit cell would predict a spread (95% confidence limits) in the expansion of 7.4 ± 1.5%. The experimental and theoretical predictions for the distribution in the expansion therefore also agree to within experimental error. The variable crystal alignment most likely results from small variations in the growth direction along the AAO pore channels. It is possible that more uniform channels would lead to more aligned nanorods and less variability in the expansion. The ability to characterize this distribution with atomic resolution in inhomogeneous samples is a salient feature of NMR-assisted crystallography.

2.4. Roadmap for engineered photomechanical response

Our results demonstrate how knowledge of the relative orientations of the **9TBAE** monomer and dimer unit cells makes it possible to quantitatively predict the magnitude of the photomechanical crystal shape change. This result presents a novel opportunity: if the initial alignment of the monomer unit cell relative to the nanorod axis could be controlled, either through self-assembly or by precision cutting from bulk single crystals,[80] a variable mechanical response could be engineered. Using the model developed here, we systematically explored different starting unit cell orientations, and found that a maximum expansion of 9% could be obtained for rods in which the monomer is arranged with its crystallographic *c* axis 15° off of the nanorod axis (Euler angles $\{\beta = 75°, \gamma = 0°\}$). This orientation nearly aligns the full butterfly expansion axis (the *ac* face diagonal in Fig. 5) along the rod axis. Alternatively, a contraction of 9.5% was found for nanorods in which the monomer crystallographic *b* axis was initially aligned along the nanorod axis. This corresponds to a rotation of the crystal in Fig. 5b by 90° about the axis perpendicular to the page.

Crystal engineering concentrates on controlling the local molecular packing within a crystal to yield desired material properties, often by varying the molecular structure through synthetic modification. The results here suggest an alternative approach – controlling the molecular orientation with respect to the macroscopic crystal shape. For **9TBAE**, our results suggest that such an approach can yield a dynamic range of nearly 20% in length change. Crystal shape engineering may be a fruitful avenue to produce photomechanical materials that generate extraordinarily large strains, even for standard photochromes that show little response in their natural habit.

Conceivably, one might hope to engineer the combination of molecular structure, crystal packing, and orientation to achieve a material with a specific dynamic range of motion. Given how even small changes in molecular structure can lead to completely different packing motifs, computational crystal structure prediction could be helpful.[81] Crystal structure prediction has recently been employed to discover materials with desired porosity[82] or organic semiconducting properties,[83,84] for example. The photomechanical materials described here would provide an even stiffer challenge, since knowledge of the crystal structure before and after the photochemical reaction is required. Crystal structure prediction for the reactant species would be relatively straightforward. On the other hand, structure prediction for the photodimer product is complicated by the fact that the crystal-to-crystal photochemical transformation can produce polymorphs that are substantially less stable than those that occur under traditional crystallization conditions.[85] This makes it hard to identify the correct photodimer product structure from the many hypothetical higher-energy crystal structures typically generated in a structure prediction study.[86] On the other hand, it might be possible to identify the photodimer structure by comparing the relationships between potential photodimer crystal packings with that of the unreacted monomer crystal. Once the crystal structures are known, one would determine the optimal crystal orientation for achieving the desired dynamic range and then design an experimental strategy for producing the crystals accordingly.

3. Conclusion

A combined solid-state NMR, diffraction, and computational approach has been used to establish the atomic-resolution, molecular mechanism for the macroscopically-observed photomechanical expansion of **9TBAE** nanorods. Key to its success was the determination of the absolute orientations of the monomer and SSRD unit cells relative to the nanorod axis. For the first time, we can precisely map out how photochemical changes shift both molecular alignment and packing in a photomechanical crystal, allowing us to predict an expansion of 7.4%, in very good quantitative agreement with the experimental value of 8%. Packing defects and disorder will affect the observed expansion of individual rods but do not appear to play a dominant role. Thus it should be possible to develop quantitative structure–function relations that can be used to optimize molecular crystal photomechanical systems. The results in this paper also point to a need for more sophisticated theoretical approaches that enable the *a priori* prediction of crystal photomechanical motions. A combination of theory and experiment should enable the design of crystalline photomechanical materials with greater energy densities and higher strains, leading to applications in photon-powered actuators from smart materials to medicine.[87] Finally, this approach points to a new use of NMR-assisted crystallography that moves beyond the description of static structures to the characterization of chemical reactivity and mechanism, a theme shared by concomitant development and emerging applications of NMR-assisted crystallography in biological chemistry.[69,88,89]

4. Experimental

4.1. Preparation of 9TBAE nanorods inside AAO templates

The **9TBAE** crystalline nanorods were grown using the solvent annealing method.[36,39] 5 mg of **9TBAE** was dissolved in 100 μL of HPLC grade tetrahydrofuran. The solution was deposited on an anodized aluminum oxide (AAO) template (Whatman Anodisc, 13 mm diameter, 60 μm thickness, 200 nm pore diameter) which was supported by a Teflon ring to allow for vapor circulation. The template and Teflon holder were then covered by a glass bell-jar along with a cotton ball saturated by THF. At room temperature, the solvent evaporated slowly inside bell jar and allowed the **9TBAE** to recrystallize inside AAO channels. After 24 hours, the template was totally dry. A 1500 grit sandpaper was used to polish away residual **9TBAE** on the template surface.

4.2. Preparation of 13C labeled 9TBAE

9TBAE was prepared with two separate ^{13}C labeling patterns as described in the ESI.† The first was ^{13}C labeled on the ester moiety *t*-butyl groups ($^{13}C_4$-*t*-Bu-**9TBAE**) and the second on the ester carbonyl group (^{13}C15-**9TBAE**).

4.3. 9TBAE nanorod expansion

Isolated nanorods and bundles were prepared by dissolving the AAO templates containing **9TBAE** nanorods in 30% phosphoric acid with 0.2 wt% SDS, leaving an aqueous suspension that could be deposited on a microscope slide. The nanorod suspension was irradiated by a 365 nm light source in an Olympus IX-70 microscope with 20 mW cm^{-2} average intensity. Nanorod expansion was observed after several seconds, and the expansion was measured by analysis of the optical images before and after irradiation.

4.4. First-principles geometries and chemical shift calculations

First-principles refined solid-state structures and chemical shifts for the **9TBAE** monomer[73] and SSRD[40] were previously reported as part of benchmarking and NMR-assisted crystallographic studies, respectively. In brief, solid-state geometry optimizations were first performed using the freely available *Quantum Espresso* (QE) software package,[90] using the PBE density functional and the D2 dispersion correction,[91] ultrasoft pseudopotentials with a plane wave cut off of 80 Ry, and a 3 × 3 × 3 Monkhorst–Pack *k*-point grid. The pseudopotentials H.pbe-rrkjus.UPF, C.pbe-rrkjus.UPF, and O.pbe-rrkjus.UPF from http://www.quantum-espresso.org were used. These structures were used for NMR chemical shift calculations, performed using a fragment-based cluster approach with fragmentation carried out using a hybrid many-body interaction code[92] and including pair-wise contributions from all molecules (asymmetric units) lying within 6 Å. Individual shielding tensor calculations were performed using Gaussian09 at the PBE0/6-311+G(2d,p) level and employing the mixed basis scheme previously reported.[73,93] In these calculations, electrostatic point-charge embedding was employed out to a radius of 30 Å. Calculated ^{13}C chemical shieldings (σ) were converted to chemical shifts (δ) using the linear rescaling relation[73,93] $\delta[\mathrm{TMS(l)}] = (-0.9674)\sigma_{\mathrm{calc}} + 179.5$. Benchmarking studies have demonstrated good agreement between experimental and computationally-predicted chemical shifts, with root-mean-square-errors (RMSE) of 1.4 ppm for isotropic shifts, 3.2 ppm for aliphatic and aromatic shift tensor components, and 9.2 ppm for tensor components of sp^2 carbons directly bonded to oxygen and nitrogen atoms.[73,93]

The crystal information files (CIF) for the **9TBAE** monomer and SSRD structures are included in the ESI,† along with a summary of the chemical shift and dipolar tensors for the relevant sites.

4.5. Oriented-crystal NMR

Solid-state ^{13}C NMR spectra of the ensemble-oriented **9TBAE** monomer and solid-state reacted dimer crystals were acquired at 9.4 T (400.37 MHz ^{1}H, 100.68 MHz ^{13}C) on a Bruker AVANCE III spectrometer equipped with a homebuilt double resonance solid-state NMR probe fitted with a static flat coil (Fig. S2†). The coil was wound in 4 turns from 2 mm wide high-oxygen free copper flat wire, with overall coil dimensions of

14 mm × 14 mm × 3 mm. The coil was positioned with the largest side perpendicular to the magnetic field and could be shimmed to a ^{13}C line width of 3 ppm on a static sample of adamantane powder. Cross-polarization was implemented using a spin lock field of 25 kHz on ^{1}H and a ramped field of 21–29 kHz on ^{13}C, with a 2 ms contact time; excitation and decoupling powers on ^{1}H were 40 kHz. The ^{13}C spectra shown consist of the sum of 8192 transients acquired with a relaxation delay of 4 s, for a total acquisition time of 9.1 h. ^{13}C chemical shifts were referenced indirectly to neat TMS *via* an external solid-state sample of adamantane with the downfield-shifted peak set to 38.48 ppm.[94]

The nanorods were oriented with their long axes parallel to the magnetic field by leaving them within the disk-shaped AAO templates and placing the disks within the flat-coil NMR probe perpendicular to the magnetic field (Fig. S2†). The nanorods grow with their rod axes normal to the disk surface,[39] so this arrangement of the coil and disk aligns the rods along the static magnetic field.

4.6. Density matrix simulations of NMR spectra

^{13}C solid-state NMR spectra were simulated using a four-spin numerical density matrix approach implemented within the Mathematica™ programming environment.[95] The $^{13}C_4$-labeled *t*-butyl group was modeled as a strongly-coupled spin system with dipolar and scalar coupling interactions between all sites. Full details are given in the ESI.†

4.7. Grazing incidence wide-angle X-ray scattering

Grazing incidence wide-angle X-ray diffraction (GIWAXS) experiments were performed using a Ganesha SAXS-LAB instrument at room temperature. X-rays ($\lambda = 1.54$ Å, Cu Kα radiation) were incident at an angle of 2° with respect to the sample surface. A slice of **9TBAE**-filled AAO template (3 mm × 1 mm) was mounted on a Thorlabs rotation Stage (MSRP01). A Pilatus 300 K detector was used to collect the 2D diffraction pattern. All the GIWAXS raw data were processed using SAXSGUI software. The monomer crystals were illuminated with 365 nm light (20 mW cm^{-2}) for 6 h to convert into dimer crystals.

Author contributions

All authors have contributed to this work with primary contributions in the follow areas. Overall research direction: Mueller, Bardeen, Beran; NMR spectroscopy: Chalek, Kudla, Yang, Magalhães, Mueller; nanorod preparation and characterization: Dong, Tong, Zhu, Al-Kaysi, Bardeen; first-principles computational chemistry: Hartman, Beran; synthetic organic chemistry: Gill, Al-Kaysi, Hooley; GIWAXS: Xu, Hayward.

Conflicts of interest

There are no conflicts to declare.

Acknowledgements

Research reported in this publication was supported by the United States National Science Foundation (DMR-1810514 to CJB, CHE-1708019 to RJH, CHE-1665212 and CHE-1955554 to GJB, CHE-1710671 to LJM), the US National Institutes of Health (GM097569 to LJM), the Office of Naval Research (MURI on Photomechanical Material Systems; ONR N00014-18-1-2624 to CJB and RCH), and KSAU-HS/KSIMRC (RC10/104 to ROK). Supercomputer time from XSEDE (TG-CHE110064 to GJB) is acknowledged and additional computations were performed using the computer clusters and data storage resources of the UCR HPCC, which were funded by grants from NSF (MRI-1429826) and NIH (1S10OD016290-01A1). The flat-coil NMR probe was constructed with the assistance of Albert Wu and the UCSD Center for Magnetic Resonance and the Imaging of Proteins supported by NIH grant P41EB002031.

References

1 R. P. Young, C. R. Lewis, C. Yang, L. Wang, J. K. Harper and L. J. Mueller, *Magn. Reson. Chem.*, 2019, **57**, 211–223.

2 P. Naumov, S. Chizhik, M. K. Panda, N. K. Nath and E. Boldyreva, *Chem. Rev.*, 2015, **115**, 12440–12490.

3 S. Chizhik, A. Sidelnikov, B. Zakharov, P. Naumov and E. B. ab, *Chem. Sci.*, 2018, **9**, 2319–2335.

4 P. Naumov, J. Kowalik, K. M. Solntsev, A. Baldridge, J.-S. Moon, C. Kranz and L. M. Tolbert, *J. Am. Chem. Soc.*, 2010, **132**, 5845–5857.

5 H. Koshima, H. Nakaya, H. Uchimoto and N. Ojima, *Chem. Lett.*, 2012, **41**, 107–109.

6 H. Koshima, N. Ojima and H. Uchimoto, *J. Am. Chem. Soc.*, 2009, **131**, 6890–6891.

7 H. Koshima, K. Takechi, H. Uchimoto, M. Shiro and D. Hashizume, *Chem. Commun.*, 2011, **47**, 11423–11425.

8 D. Kitagawa, K. Kawasaki, R. Tanaka and S. Kobatake, *Chem. Mater.*, 2017, **29**, 7524–7529.

9 D. Kitagawa and S. Kobatake, *Photochem. Photobio. Sci.*, 2014, **13**, 764–769.

10 D. Kitagawa, R. Tanaka and S. Kobatake, *Crystengcomm*, 2016, **18**, 7236–7240.

11 M. Morimoto and M. Irie, *J. Am. Chem. Soc.*, 2010, **132**, 14172–14178.

12 S. Ohshima, M. Morimoto and M. Irie, *Chem. Sci.*, 2015, **6**, 5746–5752.

13 O. S. Bushuyev, A. Tomberg, T. Friscic and C. J. Barrett, *J. Am. Chem. Soc.*, 2013, **135**, 12556–12559.

14 H. Wang, P. Chen, Z. Wu, J. Zhao, J. Sun and R. Lu, *Angew. Chem., Int. Ed.*, 2017, **56**, 9463–9467.

15 J. Liu, K. Ye, Y. Shen, J. Peng, J. Sun and R. Lu, *J. Mater. Chem. C*, 2020, ASAP.

16 D. Kitagawa, H. Nishi and S. Kobatake, *Angew. Chem., Int. Ed.*, 2013, **52**, 9320–9322.

17 D. Kitagawa, H. Tsujioka, F. Tong, X. Dong, C. J. Bardeen and S. Kobatake, *J. Am. Chem. Soc.*, 2018, **140**, 4208–4212.

18 L. Zhu, R. O. Al-Kaysi and C. J. Bardeen, *J. Am. Chem. Soc.*, 2011, **133**, 12569–12575.

19 J. M. Cole, J. d. J. Velazquez-Garcia, D. J. Gosztola, S. G. Wang and Y.-S. Chen, *Chem. Mater.*, 2019, **31**, 4927–4935.

20 F. Tong, M. Al-Haidar, L. Zhu, R. O. Al-Kaysi and C. J. Bardeen, *Chem. Commun.*, 2019, **55**, 3709–3712.

21 P. Naumov, S. C. Sahoo, B. Z. Zakharov and E. V. Boldyreva, *Angew. Chem., Int. Ed.*, 2013, **52**, 9990–9995.

22 R. Medishetty, A. Husain, Z. Bai, T. Runceviski, R. E. Dinnebier, P. Naumov and J. J. Vittal, *Angew. Chem., Int. Ed.*, 2014, **53**, 5907–5911.

23 L. Zhu, R. O. Al-Kaysi and C. J. Bardeen, *Angew. Chem., Int. Ed.*, 2016, **55**, 7073–7076.

24 E. Uchida, R. Azumi and Y. Norikane, *Nat. Commun.*, 2015, **6**, 7310/7311–7317.

25 T. Kim, L. Zhu, L. J. Mueller and C. J. Bardeen, *J. Am. Chem. Soc.*, 2014, **136**, 6617–6625.

26 N. K. Nath, L. Pejov, S. M. Nichols, C. Hu, N. Saleh, B. Kahr and P. Naumov, *J. Am. Chem. Soc.*, 2014, **136**, 2757–2766.

27 G. Liu, J. Liu, Y. Liu and X. Tao, *J. Am. Chem. Soc.*, 2014, **136**, 590–593.

28 M. K. Panda, T. Runcevski, S. C. Sahoo, A. A. Belik, N. K. Nath, R. E. Dinnebier and P. Naumov, *Nat. Commun.*, 2014, **5**, 4811–4818.

29 A. Khalil, D. P. Karothu and P. e. Naumov, *J. Am. Chem. Soc.*, 2019, **141**, 3371–3375.

30 L. Li, P. Commins, M. B. Al-Handawi, D. P. Karothu, J. M. Halabi, S. Schramm, J. Weston, R. Rezgui and P. Naumov, *Chem. Sci.*, 2019, **10**, 7327–7332.

31 H. Durr and H. Bouas-Laurent, *Photochromism : Molecules and Systems*, Elsevier, New York, 1990.

32 A. Shimamura, A. Priimagi, J.-i. Mamiya, T. Ikeda, Y. Yu, C. J. Barrett and A. Shishido, *ACS Appl. Mater. Interfaces*, 2011, **3**, 4190–4196.

33 S. Aiken, R. J. L. Edgar, C. D. Gabbutt, B. M. Heron and P. A. Hobson, *Dyes Pigm.*, 2018, **149**, 92–121.

34 A. E. Keating and M. A. Garcia-Garibay, in *Organic and Inorganic Photochemistry*, ed. V. Ramamurthy and K. S. Schanze, Dekker, New York, 1st edn, 1998, vol. 2, pp. 195–248.

35 S. Takahashi, H. Miura, H. Kasai, S. Okada, H. Oikawa and H. Nakanishi, *J. Am. Chem. Soc.*, 2002, **124**, 10944–10945.

36 R. O. Al-Kaysi and C. J. Bardeen, *Chem. Comm.*, 2006, 1224–1226.

37 D. K. Bucar and L. R. MacGillivray, *J. Am. Chem. Soc.*, 2007, **129**, 32–33.

38 L. Zhu, A. Agarwal, J. Lai, R. O. Al-Kaysi, F. S. Tham, T. Ghaddar, L. Mueller and C. J. Bardeen, *J. Mater. Chem.*, 2011, **21**, 6258–6268.

39 R. O. Al-Kaysi, A. M. Muller and C. J. Bardeen, *J. Am. Chem. Soc.*, 2006, **128**, 15938–15939.

40 C. Yang, L. Zhu, R. A. Kudla, J. D. Hartman, R. O. Al-Kaysi, S. Monaco, B. Schatschneider, A. Magalhaes, G. J. O. Beran, C. J. Bardeen and L. J. Mueller, *Crystengcomm*, 2016, **18**, 7319–7329.

41 K. D. M. Harris and J. M. Thomas, *J. Solid State Chem.*, 1991, **94**, 197–205.

42 S. G. Stitchell, K. D. M. Harris and A. E. Aliev, *Struct. Chem.*, 1994, **5**, 327–333.

43 K. Takegoshi, S. Nakamura and T. Terao, *Solid State Nucl. Magn. Reson.*, 1998, **11**, 189–196.

44 A. Hilgeroth, G. Hempel, U. Baumeister and D. Reichert, *Solid State Nucl. Magn. Reson.*, 1999, **13**, 231–243.

45 M. Bertmer, R. C. Nieuwendaal, A. B. Barnes and S. E. Hayes, *J. Phys. Chem. B*, 2006, **110**, 6270–6273.

46 R. O. Al-Kaysi, R. J. Dillon, J. M. Kaiser, L. J. Mueller, G. Guirado and C. J. Bardeen, *Macromolecules*, 2007, **40**, 9040–9044.

47 I. Fonseca, S. Hayes, B. Bluemich and M. Bertmer, *Phys. Chem. Chem. Phys.*, 2008, **10**, 5898–5907.

48 M. Khan, G. Brunklaus, V. Enkelmann and H. W. Spiess, *J. Am. Chem. Soc.*, 2008, **130**, 1741–1748.

49 R. C. Nieuwendaal, M. Bertmer and S. E. Hayes, *J. Phys. Chem. B*, 2008, **112**, 12920–12926.

50 I. Fonseca, M. Baias, S. E. Hayes, C. J. Pickard and M. Bertmer, *J. Phys. Chem. C*, 2012, **116**, 12212–12218.

51 T. Kim, L. C. Zhu, L. J. Mueller and C. J. Bardeen, *Crystengcomm*, 2012, **14**, 7792–7799.

52 T. Kim, L. C. Zhu, L. J. Mueller and C. J. Bardeen, *J. Am. Chem. Soc.*, 2014, **136**, 6617–6625.

53 R. C. Nieuwendaal, S. J. Mattler, M. Bertmer and S. E. Hayes, *J. Phys. Chem. B*, 2011, **115**, 5785–5793.

54 F. Tong, W. Xu, M. Al-Haidar, D. Kitagawa, R. O. Al-Kaysi and C. J. Bardeen, *Angew. Chem., Int. Ed.*, 2018, **57**, 7080–7084.

55 A. Nayeem and J. P. Yesinowski, *J. Chem. Phys.*, 1988, **89**, 4600–4608.

56 J. C. Facelli and D. M. Grant, *Nature*, 1993, **365**, 325–327.

57 R. A. Olsen, J. Struppe, D. W. Elliott, R. J. Thomas and L. J. Mueller, *J. Am. Chem. Soc.*, 2003, **125**, 11784–11785.

58 R. Witter, U. Sternberg, S. Hesse, T. Kondo, F. T. Koch and A. S. Ulrich, *Macromolecules*, 2006, **39**, 6125–6132.

59 G. Pintacuda, N. Giraud, R. Pierattelli, A. Bockmann, I. Bertini and L. Emsley, *Angew. Chem., Int. Ed.*, 2007, **46**, 1079–1082.

60 E. Salager, G. M. Day, R. S. Stein, C. J. Pickard, B. Elena and L. Emsley, *J. Am. Chem. Soc.*, 2010, **132**, 2564–2566.

61 C. Bonhomme, C. Gervais, F. Babonneau, C. Coelho, F. Pourpoint, T. Azais, S. E. Ashbrook, J. M. Griffin, J. R. Yates, F. Mauri and C. J. Pickard, *Chem. Rev.*, 2012, **112**, 5733–5779.

62 C. Luchinat, G. Parigi, E. Ravera and M. Rinaldelli, *J. Am. Chem. Soc.*, 2012, **134**, 5006–5009.

63 M. Baias, J. N. Dumez, P. H. Svensson, S. Schantz, G. M. Day and L. Emsley, *J. Am. Chem. Soc.*, 2013, **135**, 17501–17507.

64 D. H. Brouwer, S. Cadars, J. Eckert, Z. Liu, O. Terasaki and B. F. Chmelka, *J. Am. Chem. Soc.*, 2013, **135**, 5641–5655.

65 J. K. Harper, R. Iuliucci, M. Gruber and K. Kalakewich, *Crystengcomm*, 2013, **15**, 8693–8704.

66 L. J. Mueller and M. F. Dunn, *Acc. Chem. Res.*, 2013, **46**, 2008–2017.

67 C. Martineau, *Solid State Nucl. Magn. Reson.*, 2014, **63–64**, 1–12.

68 D. L. Bryce, *IUCrJ*, 2017, **4**, 350–359.

69 A. Bertarello, L. Benda, K. J. Sanders, A. J. Pell, M. J. Knight, V. Pelmenschikov, L. Gonnelli, I. C. Felli, M. Kaupp,

L. Emsley, R. Pierattelli and G. Pintacuda, *J. Am. Chem. Soc.*, 2020, **142**, 16757–16765.

70 M. Mehring, *Principles of high resolution NMR in solids*, Springer-Verlag, Berlin ; New York, 1983.

71 L. J. Mueller, *Concepts Magn. Reson., Part A*, 2011, **38A**, 221–235.

72 U. Haeberlen, *High resolution NMR in solids : selective averaging*, Academic Press, New York, 1976.

73 J. D. Hartman, R. A. Kudla, G. M. Day, L. J. Mueller and G. J. O. Beran, *Phys. Chem. Chem. Phys.*, 2016, **18**, 21686–21709.

74 S. J. Opella and F. M. Marassi, *Chem. Rev.*, 2004, **104**, 3587–3606.

75 R. L. Johnson and K. Schmidt-Rohr, *J. Magn. Reson.*, 2014, **239**, 44–49.

76 S. Radhakrishnan, H. Colaux, C. V. Chandran, D. Dom, L. Verheyden, F. Taulelle, J. Martens and E. Breynaert, *Anal. Chem.*, 2020, **92**, 13004–13009.

77 K. Biradha and R. Santra, *Chem. Soc. Rev.*, 2013, **42**, 950–967.

78 G. M. J. Schmidt, *Pure Appl. Chem.*, 1971, **27**, 647–678.

79 W. Shang, M. B. Hickey, V. Enkelmann, B. B. Snider and B. M. Foxman, *CrystEngComm*, 2011, **13**, 4339–4350.

80 W. Li, J. v. Baren, A. Berges, E. Bekyarova, C. H. Lui and C. J. Bardeen, *Cryst. Growth Des.*, 2020, **20**, 1583–1589.

81 A. M. Lund, G. I. Pagola, A. M. Orendt, M. B. Ferraro and J. C. Facelli, *Chem. Phys. Lett.*, 2015, **626**, 20–24.

82 A. Pulido, L. J. Chen, T. Kaczorowski, D. Holden, M. A. Little, S. Y. Chong, B. J. Slater, D. P. McMahon, B. Bonillo, C. J. Stackhouse, A. Stephenson, C. M. Kane, R. Clowes, T. Hasell, A. I. Cooper and G. M. Day, *Nature*, 2017, **543**, 657–664.

83 C. Y. Cheng, J. E. Campbell and G. M. Day, *Chem. Sci.*, 2020, **11**, 4922–4933.

84 A. N. Sokolov, S. Atahan-Evrenk, R. Mondal, H. B. Akkerman, R. S. Sanchez-Carrera, S. Granados-Focil, J. Schrier, S. C. B. Mannsfeld, A. P. Zoombelt, Z. N. Bao and A. Aspuru-Guzik, *Nat. Commun.*, 2011, **2**, 437.

85 G. J. O. Beran, *Crystengcomm*, 2019, **21**, 758–764.

86 S. L. Price, D. E. Braun and S. M. Reutzel-Edens, *Chem. Commun.*, 2016, **52**, 7065–7077.

87 *Photomechanical Materials, Composites, and Systems*, ed. T. J. White, Wiley, Hoboken, New Jersey, 2017.

88 B. G. Caulkins, R. P. Young, R. A. Kudla, C. Yang, T. J. Bittbauer, B. Bastin, E. Hilario, L. Fan, M. J. Marsella, M. F. Dunn and L. J. Mueller, *J. Am. Chem. Soc.*, 2016, **138**, 15214–15226.

89 H. L. Zhang, G. J. Hou, M. M. Lu, J. Ahn, I. J. L. Byeon, C. J. Langmead, J. R. Perilla, I. Hung, P. L. Gor'kov, Z. H. Gan, W. W. Brey, D. A. Case, K. Schulten, A. M. Gronenborn and T. Polenova, *J. Am. Chem. Soc.*, 2016, **138**, 14066–14075.

90 P. Giannozzi, S. Baroni, N. Bonini, M. Calandra, R. Car, C. Cavazzoni, D. Ceresoli, G. L. Chiarotti, M. Cococcioni, I. Dabo, A. Dal Corso, S. de Gironcoli, S. Fabris, G. Fratesi, R. Gebauer, U. Gerstmann, C. Gougoussis, A. Kokalj, M. Lazzeri, L. Martin-Samos, N. Marzari, F. Mauri, R. Mazzarello, S. Paolini, A. Pasquarello, L. Paulatto, C. Sbraccia, S. Scandolo, G. Sclauzero, A. P. Seitsonen, A. Smogunov, P. Umari and R. M. Wentzcovitch, *J. Phys.: Condens. Matter*, 2009, **21**, 395502.

91 J. Antony and S. Grimme, *Phys. Chem. Chem. Phys.*, 2006, **8**, 5287–5293.

92 G. J. O. Beran, *J. Chem. Phys.*, 2009, **130**, 164115.

93 J. D. Hartman, S. Monaco, B. Schatschneider and G. J. O. Beran, *J. Chem. Phys.*, 2015, **143**, 102809.

94 C. R. Morcombe and K. W. Zilm, *J. Magn. Reson.*, 2003, **162**, 479–486.

95 *Mathematica, version 11.2, software for technical computation*, Wolfram Research , Inc., Champaign, Illinois, 2017.